Experimental Mechanics
DOI 10.1007/s11340-009-9324-8

Digital Image Correlation for Improved Detection of Basal Cell Carcinoma

J.D. Krehbiel · J. Lambros · J.A. Viator · N.R. Sottos

Received: 7 June 2009 / Accepted: 21 December 2009

Abstract Border detection is a critical aspect during removal of a basal cell carcinoma tumor. Since the tumor is only 3% to 50% as stiff as the healthy skin surrounding it, strain concentrates in the tumor during deformation. Here we develop a digital image correlation (DIC) technique for improved lateral border detection based upon the strain concentrations associated with the stiffness difference of healthy and cancerous skin. Gelatin skin phantoms and pigskin specimens are prepared with compliant inclusions of varying shapes, sizes, and stiffnesses. The specimens with inclusions as well as several control specimens are loaded under tension, and the full-field strain and displacement fields measured by DIC. Significant strain concentrations develop around the compliant inclusions in gelatin skin phantoms, enabling detection of the tumor border to within 2% of the actual border. At a lower magnification, the lateral border between a pigskin/inclusion interface is determined within 23% of the border. Strain concentrations are identified by DIC measurements and associated with the lateral edges of the compliant inclusions. The experimental DIC protocol developed for model specimens has potential as a tool to aid in more accurate detection of basal cell carcinoma borders.

Keywords Digital image correlation · Gelatin · Pigskin · Inclusion · Border detection · Strain concentration · Skin mechanics

J.D. Krehbiel
Department of Mechanical Sciences and Engineering,
University of Illinois at Urbana-Champaign,
Champaign, IL, USA

J. Lambros (SEM member)
Department of Aerospace Engineering,
University of Illinois at Urbana-Champaign,
Champaign, IL, USA

J.A. Viator
Departments of Biological Engineering and Dermatology,
University of Missouri,
Columbia, MO, USA

N.R. Sottos
Department of Materials Science and Engineering,
University of Illinois at Urbana-Champaign,
Champaign, IL, USA

N.R. Sottos (✉, SEM member)
Beckman Institute,
405 N. Mathews Avenue MC-251,
Urbana, IL 61801-2983, USA
e-mail: n-sottos@illinois.edu

Published online: 16 January 2010

Introduction

Basal cell carcinoma (BCC) is the most common type of cancer, affecting nearly one million patients each year in the United States of America [1]. Although it rarely metastasizes, this skin cancer can be quite unsightly and painful if left untreated. Basal cell carcinoma lesions are disfiguring and can cause interruption of normal function of surrounding tissue [2]. The main cause of BCC is exposure to ultraviolet light, so this cancer typically occurs on areas of the body that receive the most sunlight: the head, face, and neck [2–6].

Standard surgical resection or Mohs' micrographic surgery are typically recommended for patients requiring BCC removal. To remove the tumor with standard surgical resection, the surgeon will excise a 1 to 3 mm margin beyond the visible tumor border [5]. If the margin of the tumor is not properly identified, recurrence for this surgery are 26% to 42% after 5 years [3]. Mohs' surgery is much

more effective than standard surgical resection with recurrence rates near 1% after 5 years [2]. However, this process is often time-consuming, and it requires the patient to lie under local anesthesia as histology is performed on the excised tumor [6–8]. A rapid technique to identify the borders of BCC could reduce recurrence rates and decrease time spent in surgery.

Basal cell carcinoma has a Young's modulus of about 52 kPa, while healthy skin has a stiffness of 100 to 2,000 kPa; thus, BCC is 3% to 50% as stiff as the healthy skin that surrounds it [9–14]. If the skin were stretched, the strain would concentrate within the tumor. Thus, strain concentrations around BCC would provide a means for identifying the tumor border.

Here, we investigate the use of digital image correlation (DIC) to evaluate strain concentrations around compliant inclusions in two model specimens: gelatin skin phantoms and pigskin. Digital image correlation is a non-contact, optical method for determining surface displacements and strains by comparing digital images taken before and after a deformation [15, 16]. Digital image correlation requires a unique pattern on the surface of the specimen, so samples are often sprayed with paint or covered with small particles. The DIC algorithm determines two displacements (u,v) in the horizontal (x) and vertical (y) directions, respectively, and four displacement gradients $\left(\frac{\partial u}{\partial x},\frac{\partial u}{\partial y},\frac{\partial v}{\partial x},\frac{\partial v}{\partial y}\right)$. For small deformations $\frac{\partial u}{\partial x}=\varepsilon_{xx}$, $\frac{\partial v}{\partial y}=\varepsilon_{yy}$, and $\left(\frac{\partial u}{\partial y}+\frac{\partial v}{\partial x}\right)=\gamma_{xy}$, where ε_{xx}, ε_{yy}, and $2\gamma_{xy}$ are the in-plane strain tensor components.

While it was developed for structural engineering applications, DIC has recently been used to quantify deformation of biological tissue [17–20]. Elastography is another method being researched to detect the presence of tumors based upon the mechanical properties of cancer; however, elastography requires an expensive ultrasound machine, and the results are often tedious to analyze. In contrast, DIC is relatively inexpensive, and the results are easier to interpret.

Skin phantoms and pigskin specimens with compliant inclusions are fabricated to simulate the mechanical properties of human skin with BCC. Gelatin is derived from biological tissue, and its mechanical properties depend on the concentration and Bloom number of the gelatin. Bloom number is a standard measure of the gelatin strength [21]. Due to its biocompatibility and its variability of mechanical properties, gelatin has been used to simulate many tissues [22–25]. Pigskin is also a good simulant for human skin since the mechanical properties of pigskin are similar to human skin [26]. In this study the model skin samples were loaded under tension and the resulting strains and displacements during deformation were evaluated via DIC. The strain concentrations associated with the compliant inclusion enabled identification of the lateral inclusion/matrix interface.

Materials and Experimental Methods

Gelatin Stiffness Characterization

Gelatin was obtained at two separate Bloom numbers: 50 and 225 Bloom (Sigma Aldrich Chemicals and MP Biomedicals). The gelatin was prepared for testing by heating a beaker of deionized water to 60°C on a stirrer/hotplate. As the solution was stirred at 400 rpm, the gelatin powder was slowly poured into the beaker. Solutions were stirred for 20 min to allow the gelatin to dissolve. The solution was then poured into a silicone rubber mold, covered with a glass slide to prevent drying, and allowed to cool at 8°C for 24 h.

Gelatin solutions with concentrations of 5, 10, 15, 20, and 30 g/100 ml and Bloom numbers of 50 and 225 Bloom were prepared for testing in a dynamic mechanical analyzer (DMA). For samples with concentrations of 30 g/100 ml, the gelatin solution was allowed to sit unstirred for 2 min prior to pouring in the mold. This method allowed the bubbles created by the stirring process to rise out of the gelatin. After the 24 h of cooling, the glass plate was removed from the mold, and cylindrical disks 14.5 mm in diameter were punched from the gelatin sheet. The samples were approximately 2.9 mm thick.

These specimens were then tested by dynamic mechanical analysis (TA Instruments, RSA III). The gelatin cylinders were placed on the lower compression plate and the top plate was lowered until it just touched the sample. To ensure the top plate maintained contact with the sample during testing, a preload, proportional to the concentration of the gelatin, was applied to the samples prior to testing. That is, the 5 g/100 ml gelatin was loaded with a preload of 0.05 N; the 10 g/100 ml gelatin was loaded with a preload of 0.10 N, etc. The samples were then loaded at 0.1% strain and 1.5 Hz and the elastic storage modulus, E′, measured for each sample. Tests were performed under ambient conditions: 22°C and 45% relative humidity. At least five different samples were tested at each Bloom number and concentration.

Pigskin Stiffness Characterization

Pig back skin was obtained from a 1-year-old male pig sacrificed for the Animal Sciences Department at the University of Illinois. The hair and fat were carefully removed from the skin using a razor blade, leaving only the dermis and epidermis.

Sample dimensions were marked on the skin prior to cutting the skin with a razor blade. Although the samples were marked as 10 mm long with a gage length of 40 mm, the skin relaxed after being cut. Therefore, the actual samples were 8.9±0.8 mm wide with a gage length of 39.3±

2.3 mm. The thickness of the skin was 2.6±0.2 mm. To increase friction within the grips, we adhered sandpaper endtabs to the samples with cyanoacrylate cement. Samples were loaded in tension under displacement control at a rate of 10 μm/s with the apparatus shown in Fig. 1.

Skin orientation may affect the stiffness of the skin [13, 27]. Thus, eight samples were prepared with axial orientation and eight samples were prepared with transverse orientation. The skin was loaded in uniaxial tension at a rate of 10 μm/s until the samples slipped in the grips or the machine reached its maximum load. These samples were tested approximately 36 h after sacrifice. When the skin was not being prepared for testing, it remained in the refrigerator at 8°C. The skin was tested at the ambient temperature of 23°C.

DIC of Gelatin Skin Phantoms

Two control sample geometries were used to assess the accuracy of DIC on gelatin skin phantoms: gelatin with no defects and gelatin with a cylindrical hole through it. The samples with no defects were 40 mm long, 10 mm wide, and 2 mm thick. The hole was 500 μm in diameter and located in the center of the sample. The samples with the hole were the same width and thickness as samples with no defects but were 60 mm long. Gelatin samples were also prepared with compliant inclusions of varying shapes, sizes, and stiffnesses. All inclusion samples were 60 mm long, 10 mm wide, and 2 mm thick. Circular inclusions were prepared with diameters of 0.5, 2, and 5 mm. A rectangular inclusion 0.5 by 1 mm was also created. The ratio of the stiffness of the inclusion to the surrounding matrix (E_i/E_m) was 0.03 for previously mentioned inclusions. A circular inclusion with a 2 mm diameter was also created with a 0.60 stiffness ratio. A minimum of five specimens were tested for each type.

For the no defect specimens, a sheet of 225 Bloom gelatin at a concentration of 30 g/100 ml was prepared as described in the section on gelatin stiffness characterization, and the samples were cut from the sheet using a razor blade. For the cylindrical hole sample and inclusion samples, an aluminum mold was designed to create the specimens, each with an appropriate size hole in the center. A 30 g/100 ml mixture of 225 Bloom gelatin was poured into the mold, and each sample was covered with a silicone rubber sheet to prevent drying. The samples were cooled at 8°C overnight.

For the control samples, after the gelatin had set, the samples were carefully removed from the mold and sandpaper endtabs were adhered to the ends of each sample to increase friction at the grips. For the samples with inclusions, after the gelatin had set, a compliant gelatin was prepared and syringed into the hole in the 225 Bloom gelatin and allowed to cool. Inclusions of two different stiffnesses were investigated. The 5 g/100 ml 50 Bloom gelatin had a modulus of 7 kPa and produced a stiffness ratio of 0.03. The 15 g/100 ml 225 Bloom gelatin (E'= 150 kPa) provided a 0.60 stiffness ratio. Most experiments were performed with the more compliant inclusion (0.03 stiffness ratio). We then adhered sandpaper endtabs to these samples as well. Digital image correlation requires a unique speckle pattern for correlation, so samples were air-brushed with black India ink using an Iwata Custom Micron CM-B airbrush.

These gelatin skin phantoms were loaded in tension under displacement control at a rate of 10 μm/s with the apparatus shown in Fig. 1. The stage was purchased from Ernest F. Fullam Inc. (No. 18238, Tensile Testing Substage FEI XL30). A specimen was held by the flat-face grips as the motor forced the screws apart. Displacement and load data were gathered from the displacement sensor (Vishay Micro-Measurements HS50) and load cell

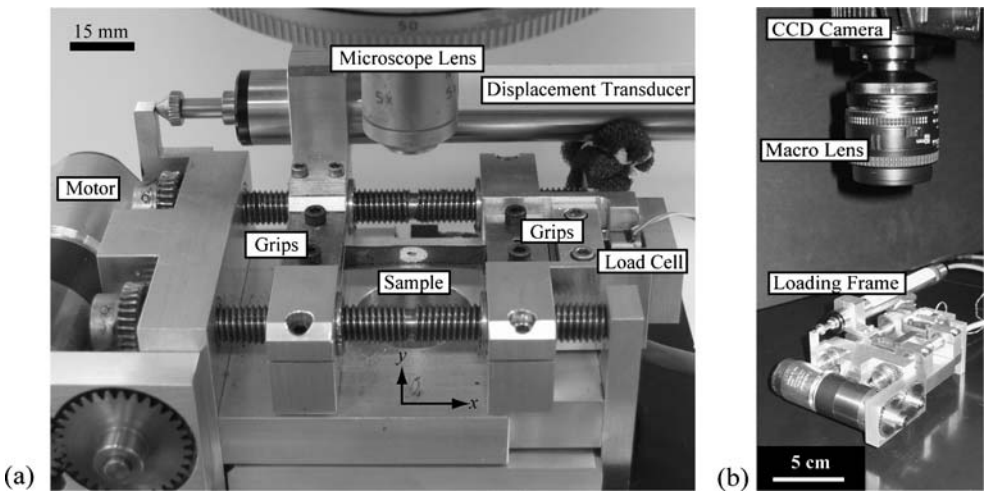

Fig. 1 Loading frame for DIC tension tests. (**a**) High magnification setup. (**b**) Low magnification setup. The sample was held by the grips which were forced apart by the motor. The displacement transducer allowed acquisition of displacement data and the load cell allowed acquisition of load data. A CCD camera mounted on top of the optical microscope (**a**) or macro lens (**b**) was used to collect images. Loading occurred in the *x*-direction

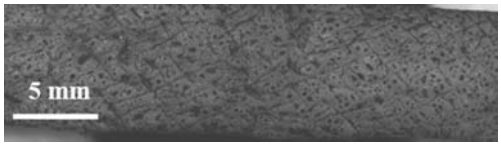

Fig. 2 Speckle pattern on pigskin

(1,000 g, Honeywell Sensotec Model 11), respectively. All instrumentation was controlled by a LabVIEW (National Instruments) program.

Images were acquired using a QImaging Retiga monochrome CCD camera with a resolution of 1,280 by 1,024 pixels. For imaging the 500 μm circular inclusion and the rectangular inclusion, the camera was mounted on a Leica DMR optical microscope with 50× magnification. The spatial resolution of the camera under this magnification was determined by imaging a resolution target. At this magnification the resolution was 2.03 μm/pixel, which allowed for a field of view of 2.08 by 2.60 mm. To image larger circular inclusions, the camera was placed on a macrolens over the loading frame [Fig. 1(b)]. Under this low magnification, the resolution was approximately 20 μm/pixel. Images were acquired before and after gelatin samples were loaded under tension at the rate of 10 μm/s to a known far-field strain, ε_0. Unless otherwise specified, the far-field strain was ε_0=1.0%.

Correlation was provided by an in-house DIC program that had been verified and calibrated to ensure it accurately measures strains and displacements [28–31]. This code used a coarse-fine search coupled with a Newton–Raphson scheme. A subset size of 31 by 31 pixels (63 by 63 μm at high magnification, 600 μm by 600 μm at low magnification) was deemed appropriate for correlation over an area of interest 700 pixels high by 900 pixels wide. Subsets were centered on every 10th pixel in this region.

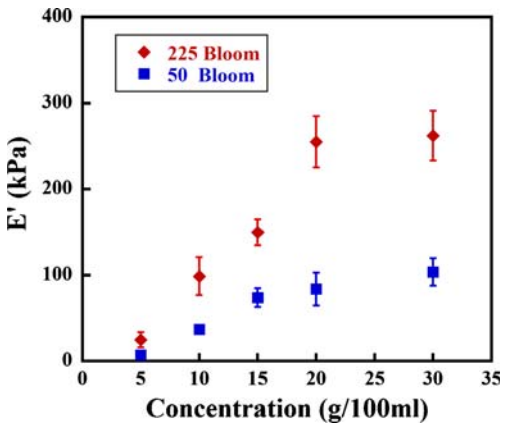

Fig. 3 Effect of concentration and Bloom number on gelatin storage modulus from DMA compression tests. Data points correspond to the average results from at least five samples tested at 1.5 Hz and 0.1% strain. Error bars correspond to one standard deviation from the mean

DIC of Pigskin Specimens

Digital image correlation testing was performed on the same pigskin lot as used for stiffness characterization. Sample preparation was identical for both of these tests. Sandpaper endtabs were adhered to the pigskin. The samples were approximately 2 mm thick by 9 mm wide with a gage length of 40 mm. As for the gelatin samples, the pigskin was air-brushed with black India ink to create the speckle pattern (Fig. 2).

Two different pigskin sample types were prepared: control samples with no defects and samples with a compliant inclusion. A hole was created in the skin by punching a hole in the skin with a leather punch. The hole was filled with vacuum grease to create a compliant inclusion. The stiffness of the grease was 100 kPa, as determined through dynamic mechanical analysis.

Samples were loaded in tension in the apparatus shown in Fig. 1 at a rate of 10 μm/s to a far-field strain of 1.0%. Images were acquired under low magnification before and after deformation. We evaluated the deformation through the in-house DIC code. The sample with no defects was tested 48 h after sacrifice. Since a suitable method for creating a compliant inclusion was not determined prior to obtaining the skin, the skin was kept frozen until these samples were prepared 43 days after sacrifice.

Results

Gelatin Stiffness Characterization

For the compression tests, the DMA software was used to determine the storage modulus, E', of each sample. Average stiffnesses were calculated for each concentration and Bloom number. Standard deviations were also measured. A graph of the storage modulus as a function of concentration of gelatin is shown in Fig. 3, and a table of these values is given in Table 1. As expected, the stiffness of the gelatin samples increases with increasing concentra-

Table 1 Average gelatin storage moduli calculated from DMA compression data

Concentration (g/100ml)	E′ (kPa)	
	50 Bloom	225 Bloom
5	7.4±1.4	25±8.7
10	37±3.4	99±22
15	74±11	150±15
20	84±19	255±30
30	104±16	262±29

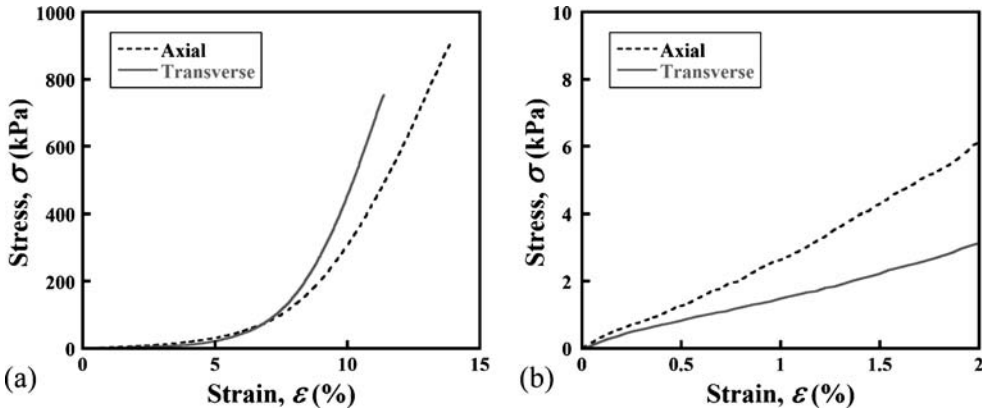

Fig. 4 Representative stress–strain curves for pigskin with different orientation. (**a**) Data between 0% and 15% strain, and (**b**) data between 0% and 2% strain

tion and increasing Bloom number. This data is in agreement with previous studies indicating Young's modulus for gelatin is between 2 and 900 kPa depending upon concentration [22, 25, 32, 33]. We were able to prepare gelatin with stiffnesses between 7 and 262 kPa to suitably simulate the stiffness ratio of BCC to healthy skin.

Pigskin Stiffness Characterization

Representative stress–strain curves for pigskin are shown in Fig. 4(a). Young's modulus was evaluated as the slope of the curve for strains less than 2% [Fig. 4(b)]. The average stiffness of axially oriented pigskin was 289±155 kPa, while the average stiffness of transversely oriented pigskin was 138±55 kPa. There is a significant amount of variability in these numbers; however, biological materials have inherent variability in their properties. Previously published work also indicates an increased modulus for skin with an axial orientation [13, 27]. The increased stiffness in the axial direction is attributed to the preferential alignment of collagen fibers along this direction.

DIC of Gelatin Skin Phantoms

Displacements were evaluated for gelatin skin phantoms via DIC. To improve the quality of the displacement results, a smoothing algorithm was added to the DIC code. For each 3 by 3 subset region, an average displacement was

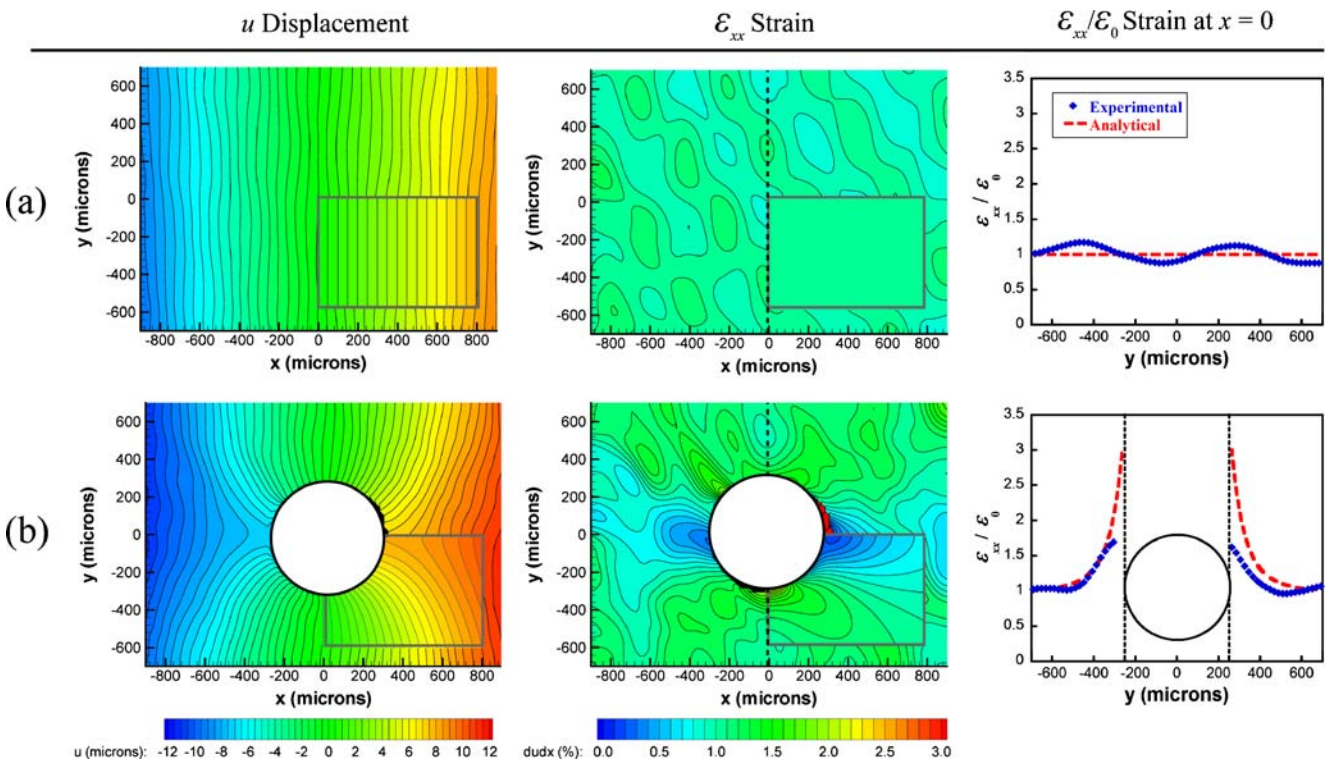

Fig. 5 Contour plots of displacements and strains from control gelatin specimens. Line scan of strain data at $x = 0$. Analytical solutions for displacements and strains are plotted in the insets in the lower right corner of the contour plots

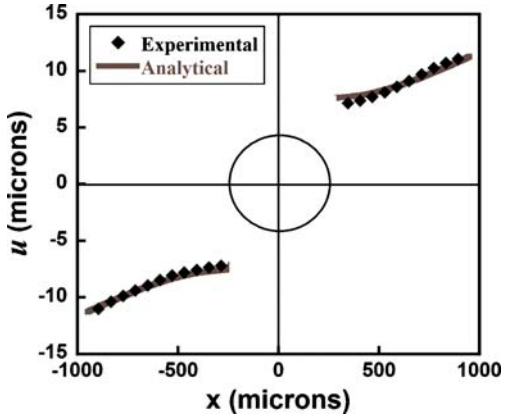

Fig. 6 Comparison of u displacements as predicted from the analytical solution for a plate with a hole in it under far-field tension and the experimental results gathered from DIC on a gelatin sample. Displacements are evaluated at $y = 0$

calculated and assigned to the value for the center subset. This process was repeated 20 times to obtain the smoothed data. While strains could be evaluated directly from DIC, numerical differentiation of the displacement data provided a more accurate measure of strain [34]. Thus, the strains were evaluated by differentiating the displacements using a 5-point finite difference scheme [35].

The u displacements and ε_{xx} strain contours for the control specimens are given in Fig. 5. The inset in the lower right in the contour plots and the red line on the line scans show the respective analytical solutions. Excellent agreement is obtained everywhere for the sample with no defects [Fig. 5(a)]; the strain is approximately equal to 1.0% everywhere in the field of view. The sample with a hole [Fig. 5(b)] was compared to the analytical solution for a hole in an infinite plate under far-field tension. That solution is given in Muskhelishvili [36], and the details of the comparison are in Krehbiel [37]. For the analytical calculations, we assume that the gel is linear elastic for the small strains applied, the Young's modulus is approximately equal to the storage modulus (E′), and that the gelatin is nearly incompressible (Poisson's ratio, $\nu = 0.49$). A clear strain concentration is obtained directly above and below the hole. The DIC strains are lower than the analytical solution near the hole. The comparison of the u displacements around the hole is shown in Fig. 6. Although the experimental DIC values for displacements correspond closely with the theoretical displacements, the smoothing and differentiation processes lead to inaccurate strain values near the edge of the hole.

The displacements and strains around circular and rectangular inclusions are given in Fig. 7. The u displacement contours bow in toward the inclusion. The maximum and minimum values of the $\frac{\partial u}{\partial y}$ displacement gradient bound the opposite edges of both inclusions. A clear ε_{xx} strain concentration is present at the left and right edges of both

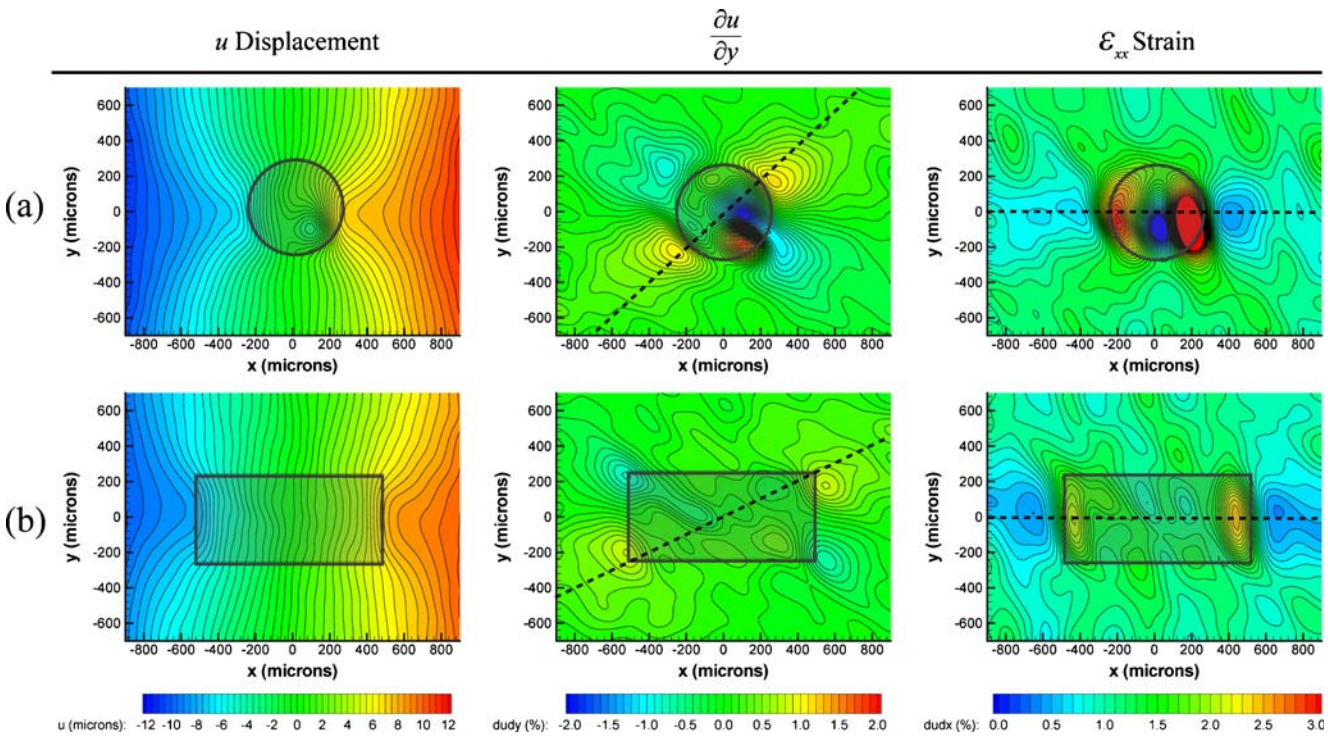

Fig. 7 The u displacement, $\frac{\partial u}{\partial y}$ displacement gradient, and ε_{xx} strain contour plots for gelatin skin phantoms of (**a**) circular and (**b**) rectangular inclusion geometry. The darkened shapes denote the location of the inclusion. The dashed lines denote the line scan of data presented in Fig. 8

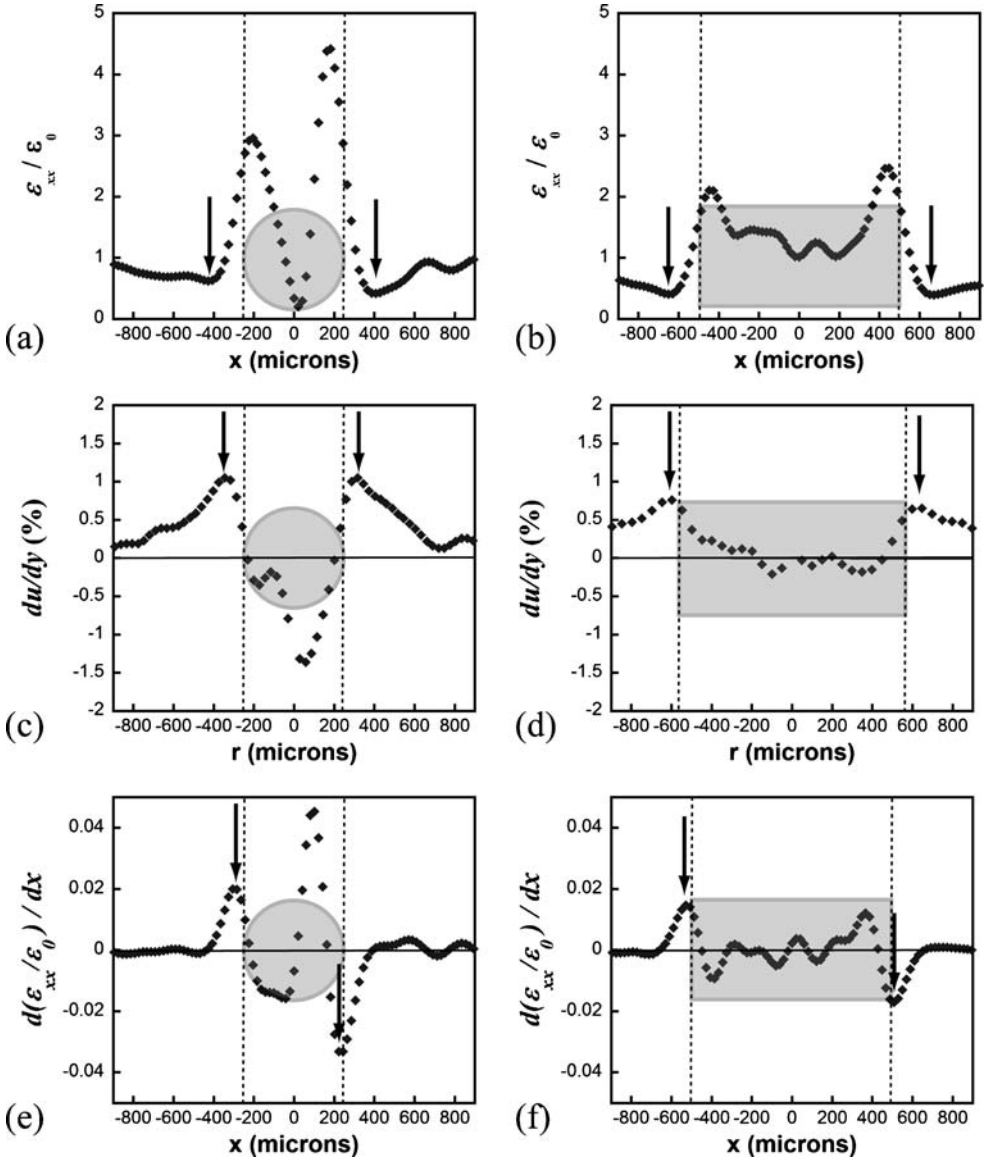

Fig. 8 Line scan of ε_{xx} data for (**a**) circular and (**b**) rectangular inclusions in gelatin skin phantoms. Line scan of $\partial u/\partial y$ data for (**c**) circular and (**d**) rectangular inclusions in gelatin skin phantoms. Line scan of $\partial\varepsilon_{xx}/\partial x$ data for (**e**) circular and (**f**) rectangular inclusions in gelatin skin phantoms. The arrows denote the location of zero slope used to calculate the border of the inclusion and matrix. Line scans taken along dashed lines shown in Fig. 7

inclusions. To estimate the border of the inclusion from the DIC results, we calculated the points of zero slope of the ε_{xx}, $\frac{\partial u}{\partial y}$, and $\partial\varepsilon_{xx}/\partial x$ line scans (Fig. 8). The strain gradient $\partial\varepsilon_{xx}/\partial x$ was calculated by differentiating the ε_{xx} data, and a line scan of this derivative is also given in Fig. 8. Table 2 expresses the location of the edge as determined from these three line scans, and the points of zero slope in each line scan are used to calculate the edges. The error for each edge calculation is shown as a percentage. The size is also calculated from the left and right edges, and a percentage

Table 2 Edge detection of gelatin skin phantoms with compliant inclusions of different shapes. Locations of zero slope in the line scan of displacement and strain gradients (Fig. 8) were used to calculate the edges

		Actual Edge (μm)	Left Edge (μm)	Left Edge Error (%)	Right Edge (μm)	Right Edge Error (%)	Size Error (%)
Filled Hole	ε_{xx}	250	−430	72	410	64	68
	$\partial u/\partial y$	250	−350	40	320	28	34
	$\partial\varepsilon_{xx}/\partial x$	250	−310	24	240	4	10
Filled Slit	ε_{xx}	500	−650	30	670	34	32
	$\partial u/\partial y$	560	−600	7	650	16	12
	$\partial\varepsilon_{xx}/\partial x$	500	−530	6	510	2	4

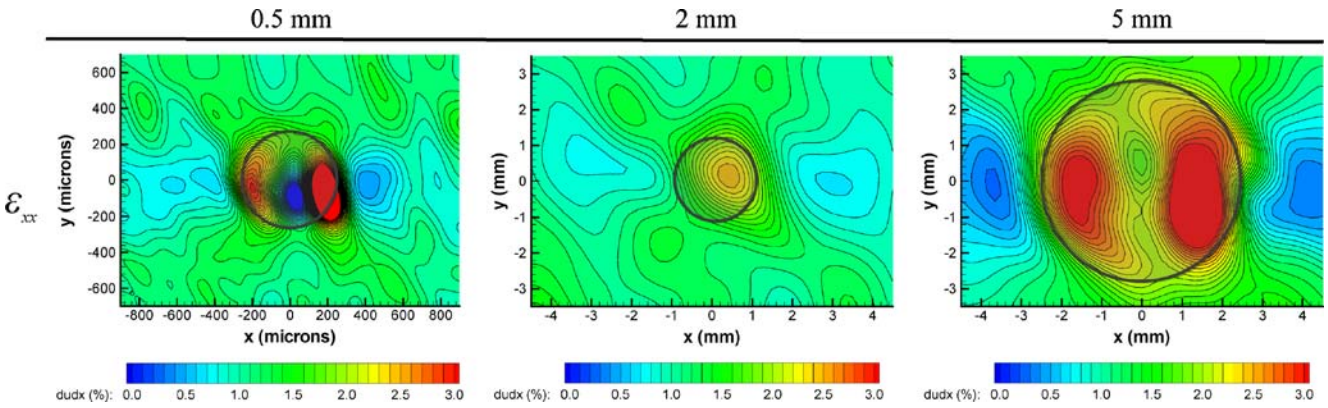

Fig. 9 Strain contour plots for inclusions with diameters of 0.5, 2, and 5 mm in a gelatin matrix

error is shown for each of the methods and samples. The data show that using the derivative of the strain as a means for calculating edges is more accurate than the other two methods. In fact, the error for edge detection with this method may be as low as 2%, and the size error as low as 4%.

We show the ε_{xx} strain contour plots for circular inclusions with diameters of 0.5, 2, and 5 mm in Fig. 9. The smallest inclusion was imaged under 50× magnification; the other inclusions were imaged under low magnification. The size of the strain concentration scales with the size of the inclusion.

The effect of the inclusion stiffness on the strain concentration was evaluated through experimental DIC tests and from theoretical predictions. An analytical solution is given in Muskhelishvili [36] for a circular inclusion in an elastic plate under far-field tension. This solution shows that the magnitude of the strain concentration also depends upon the stiffness ratio of the inclusion to the matrix. The experimental DIC results and the analytical solution for circular inclusions with stiffness ratios of 0.03 and 0.60 are given in Fig. 10. We present the normalized strain $\varepsilon_{xx}/\varepsilon_0$ because ε_0=1.0% for the sample with E_i/E_m=0.03 and ε_0=0.86% for the sample with E_i/E_m=0.60.

The analytical solution predicts the magnitude of the strain concentration to be 2.82 for E_i/E_m=0.03 and 1.36 for E_i/E_m=0.60. The DIC results show strain concentrations of 2.5 and 1.4, respectively for these two stiffness ratios. Thus a fairly good comparison is obtained for both sample types. The analytical solution predicts a steep strain increase at the

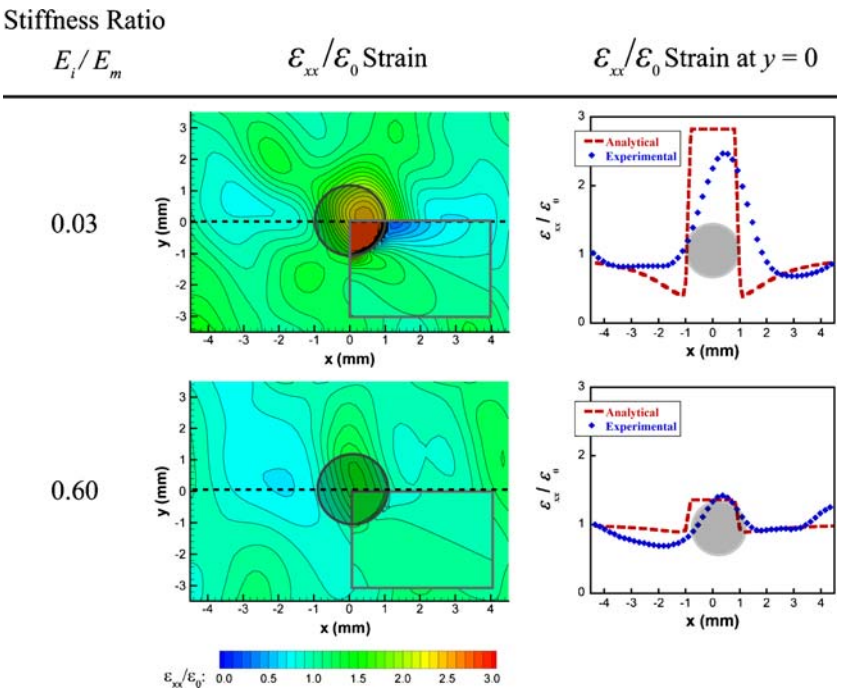

Fig. 10 Normalized strains around inclusions with different stiffness ratios. Line scan of strain data at y=0. Data from analytical solution plotted in the inset of the contour plots

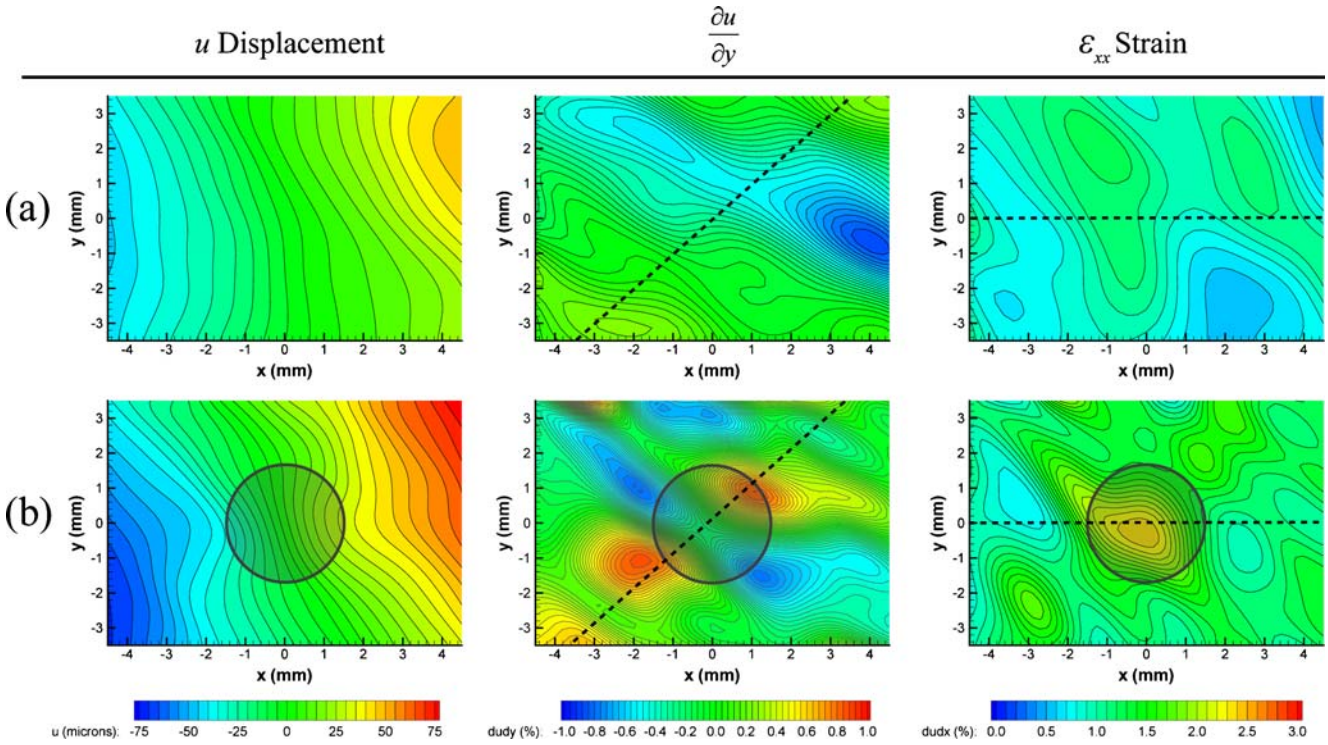

Fig. 11 Displacements and displacement gradients in pigskin with (**a**) no defects and (**b**) a compliant inclusion. The darkened geometry denotes the location of the inclusion. The dashed lines denote the line scan of data presented in Fig. 12

border between the inclusion and the matrix. This border becomes blurred in the DIC results due to the smoothing and differentiation processes that produce the strain data.

DIC of Pigskin Specimens

The u displacement, ε_{xx} strain, and $\frac{\partial u}{\partial y}$ displacement gradient contour plots for the two pigskin samples are shown in Fig. 11. The displacements for the sample with no defects show the heterogeneous nature of skin; the contours are not as evenly-spaced as for the gelatin skin phantoms (Fig. 5). The ε_{xx} strains in Fig. 11(a) show areas of slight strain concentrations in this sample created by the natural features and imperfections of the skin. However, as shown in Fig. 11(b), significant differences are noted between the sample with no defects and the skin with a compliant inclusion. The contour lines bow in toward the location of the inclusion. At the location of the compliant inclusion, an ε_{xx} strain concentration is noticeable. The $\frac{\partial u}{\partial y}$ displacement gradients exhibit high and low regions that bound the edges of the inclusion.

Line scans were taken through ε_{xx} and $\frac{\partial u}{\partial y}$ data for the two pigskin samples. The ε_{xx} strains were evaluated along $y=0$ mm; the $\frac{\partial u}{\partial y}$ displacement gradients were evaluated along a 45° line to the x-axis (Fig. 11). The strain gradient $\partial\varepsilon_{xx}/\partial x$ was also calculated by differentiating the ε_{xx} strain. These line scans are shown in Fig. 12. The strains are approximately equal to the far-field strains for the sample with no defects. Similar to the gelatin skin phantoms, the compliant inclusion creates a significant strain increase at the interface with the surrounding pigskin matrix. Here, the strain in the inclusion is 2.4 times the far-field strain. The border of the inclusion and the pigskin was evaluated as the location of zero slope in the ε_{xx} and $\frac{\partial u}{\partial y}$ displacement gradients and in the $\partial\varepsilon_{xx}/\partial x$ strain gradient. The edge detection using these three methods is shown in Table 3. Using the $\frac{\partial u}{\partial y}$ displacement gradient, we were able to estimate the location of the edge to within 19% error and the size of the inclusion to within 2% error. The strain gradient $\partial\varepsilon_{xx}/\partial x$ was also accurate in determining the size.

Discussion and Conclusions

In this study, we characterized the stiffness of gelatin through dynamic compression tests. The stiffness of the gel was altered significantly by varying the gelatin concentration and Bloom number. The data was in agreement with other research on the stiffness of gelatin. Gelatin with stiffness ratios between 0.03 and 0.50 were easily prepared and the stiffness difference between healthy and cancerous skin was suitably simulated.

We evaluated the stiffness of pigskin through uniaxial tension tests on excised pig back skin. The orientation of

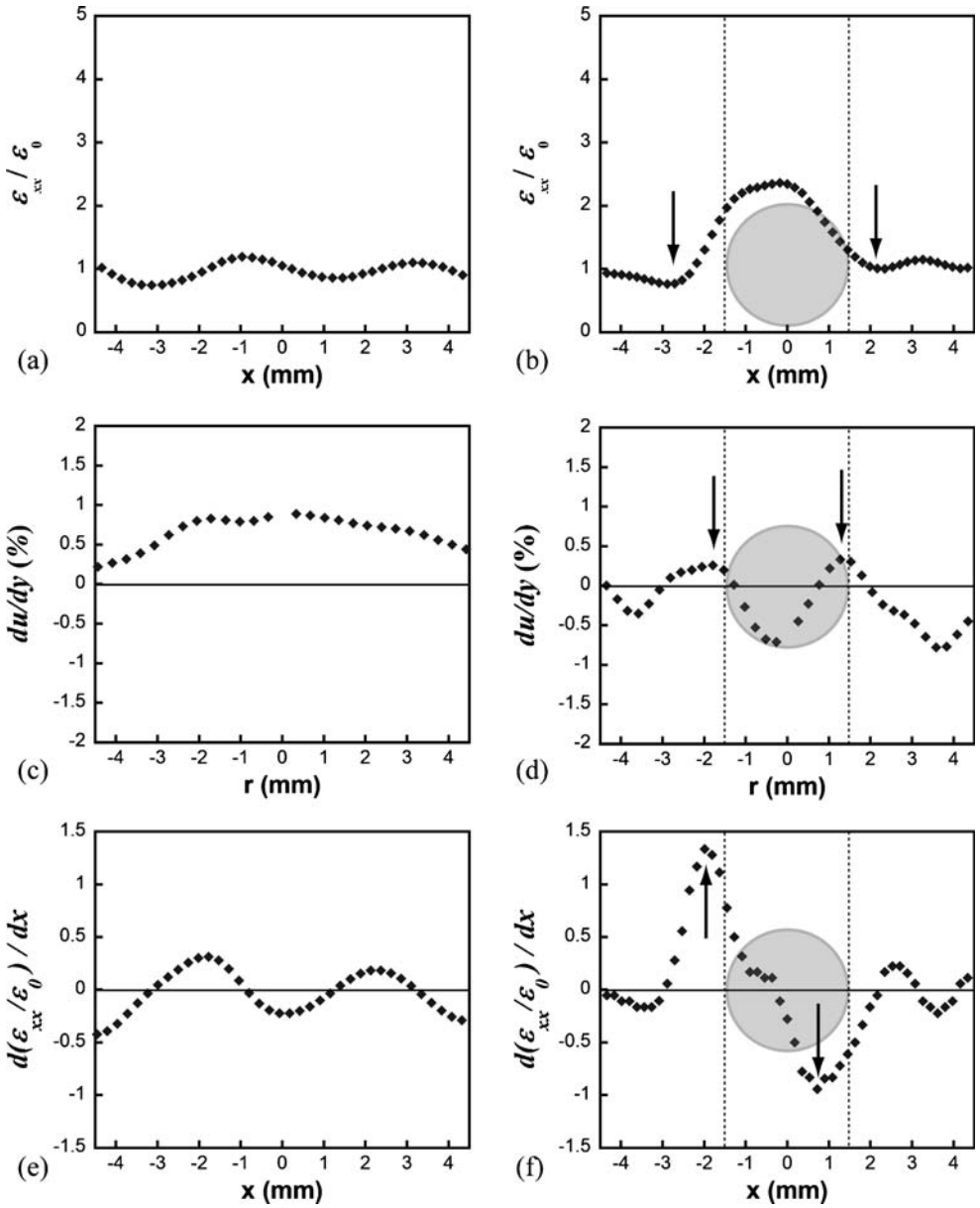

Fig. 12 Line scans of ε_{xx} strains at y=0 for pigskin with (**a**) no defects and (**b**) a compliant inclusion. Line scan of $\partial u/\partial y$ data for pigskin with (**c**) no defects and (**d**) a compliant inclusion. Line scan of $\partial \varepsilon_{xx}/\partial x$ data for pigskin with (**e**) no defects and (**f**) a compliant inclusion. The arrows denote the location of zero slope used to calculate the border of the inclusion and matrix. Line scans are taken along dashed lines shown in Fig. 11

the skin was shown to affect the stiffness of the skin. The modulus of axially oriented skin was 289±155 kPa, and the modulus of transversely oriented skin was 138±55 kPa. These results are in agreement with previous research reporting an orthotropic response for skin [13, 27].

Gelatin control specimens were prepared for tension tests, and DIC was used to evaluate the strains and displacements during deformation. For gelatin with no defects, the strains measured by DIC were in good agreement with the applied far-field strains. Additionally,

Table 3 Edge detection of a compliant circular inclusion in pigskin. Locations of zero slope in the line scan of displacement and strain gradients (Fig. 12) were used to calculate the edges

	Actual Edge (μm)	Left Edge (μm)	Left Edge Error (%)	Right Edge (μm)	Right Edge Error (%)	Size Error (%)
ε_{xx}	1,500	−2,900	93	2,350	57	75
$\partial u/\partial y$	1,500	−1,790	19	1,280	15	2
$\partial \varepsilon_{xx}/\partial x$	1,500	−1,990	33	720	52	10

the experimental displacements and strains corresponded to analytical values around a hole in an infinite plate under far-field tension. Thus, DIC provided an effective and reliable method for computing surface strains on gelatin skin phantoms.

We also evaluated the strain concentrations around compliant inclusions in gelatin. These inclusions had various shapes, sizes, and stiffnesses. Significant ε_{xx} strain concentrations were generated at the border between a stiff matrix and a compliant inclusion. Examination of the different strain components enabled identification of the *lateral* border between matrix and inclusion to within 2% of the actual border. Although varying inclusion shapes exhibited unique strain fields, in all cases displacement contours were bowed toward the inclusion and local strain minima and maxima were present at opposing edges of the inclusion boundaries. Inclusions with varying sizes also revealed strain concentrations scale with inclusion size. Although not shown explicitly, the stiffness of the inclusion could be extracted from the magnitude of the strain concentration [36]. Therefore, DIC measurements have potential for identifying the *lateral* shape, size, and stiffness of compliant inclusions.

We ran additional DIC experiments on pigskin samples. Images acquired from tensile tests on pigskin samples with different defects were correlated using DIC, and the results showed unique strain concentrations depending upon the defect. Compliant inclusions created significant strain concentrations at the inclusion/matrix interface. This interface was calculated within 19% of the actual *lateral* border via DIC measurements. The current method for surgical excision involves excision of up to 3 mm beyond the border of a tumor. For a tumor with radius of 3 mm, this process creates a 100% error in estimating the margin. A 19% margin represents a significant improvement in border detection.

Basal cell carcinoma creates a compliant inclusion in healthy skin. The strain concentrations that result from deforming an area around a compliant inclusion could prove useful in identification of the tumor border. Digital image correlation provides a simple, inexpensive method for evaluating these surface strains. We have demonstrated that compliant inclusions can be detected in gelatin skin phantoms and *ex vivo* pigskin through DIC. Further work may show that DIC could be used to locate subsurface BCC tumors as well. Thus, digital image correlation is a promising tool to aid in the detection of basal cell carcinoma.

References

1. Jemal A, Siegel R, Ward E, Murray T, Xu J, Smigal C et al (2007) Cancer Statistics, 2007. CA Cancer J Clin 57(1):43–46
2. Lin SJ, Lee SH (2006) Discrimination of basal cell carcinoma from normal dermal stroma by quantitative multiphoton imaging. Opt Lett 31:489–498
3. Ceilley RI, Del Rosso JQ (2006) Current modalities and new advances in the treatment of basal cell carcinoma. Int J Dermatol 45(5):489–498
4. Crowson AN (2006) Basal cell carcinoma: biology, morphology, and clinical implications. Mod Pathol 19:S127–S147
5. Heckmann M, Zogelmeier F, Konz B (2002) Frequency of facial basal cell carcinoma does not correlate with site-specific UV exposure. Arch Dermatol 138(11):1494–1497
6. Patel YG, Nehal KS, Aranda I, Li Y, Halpern AC, Rajadhyaksha M (2007) Confocal reflectance mosaicing of basal cell carcinomas in Mohs surgical skin excisions. J Biomed Opt 12(3):034027–10
7. Olmedo JM, Warschaw KE, Schmitt JM, Swanson DL (2006) Optical coherence tomography for the characterization of basal cell carcinoma *in vivo*: a pilot study. J Am Acad Dermatol 55 (3):408–412
8. Rajadhyaksha M, Menaker GM, Gonzalez S, Zavislan JM, Dwyer PJ (2001) Confocal cross-polarized imaging of skin cancers to potentially guide Mohs micrographic surgery. Optics Photonics News 12(12):30
9. Agache PG, Monneur C, Leveque JL, Rigal J (1980) Mechanical properties and Young's modulus of human skin *in vivo*. Arch Dermatol 269(3):221–232
10. Daly CH, Odland GF (1979) Age-related changes in the mechanical properties of human skin. J Invest Dermatol 73 (1):84–87
11. Diridollou S, Patat F, Gens F, Vaillant L, Black D, Lagarde JM et al (2000) *In vivo* model of the mechanical properties of the human skin under suction. Skin Res Technol 6(4):214
12. Escoffier C, de Rigal J, Rochefort A, Vasselet R, Leveque J-L, Agache PG (1989) Age-related mechanical properties of human skin: an *in vivo* study. J Invest Dermatol 93(3):353–357
13. Manschot JFM, Brakkee AJM (1986) The measurement and modelling of the mechanical properties of human skin *in vivo*. II. The model. J Biomech 19(7):517–521
14. Tilleman TR, Tilleman MM, Neumann MHA (2004) The elastic properties of cancerous skin: Poisson's ratio and Young's modulus. Isr Med Assoc J 6(12):753–755
15. Peters WH, Ranson WF (1982) Digital imaging techniques in experimental stress analysis. Opt Eng 21(3):427–431
16. Peters WH, Ranson WF, Sutton MA, Chu TC, Anderson J (1983) Application of digital image correlation methods to rigid body mechanics. Opt Eng 22(6):738–742
17. Marcellier H, Vescovo P, Varchon D, Vacher P, Humbert P (2001) Optical analysis of displacement and strain fields on human skin. Skin Res Technol 7(4):246
18. Staloff IA, Guan E, Katz S, Rafailovitch M, Sokolov A, Sokolov S (2008) An *in vivo* study of the mechanical properties of facial skin and influence of aging using digital image speckle correlation. Skin Res Technol 14(2):127–134
19. Thompson MS, Schell H, Lienau J, Duda GN (2007) Digital image correlation: a technique for determining local mechanical conditions within early bone callus. Med Eng Phys 29(7):820–823
20. Zhang DS, Arola DD (2004) Applications of digital image correlation to biological tissues. J Biomed Opt 9(4):691–699
21. Ward AG, Sanders PR (1958) The rheology of gelatin. In: Eirich FR (ed) Rheology, theory and applications. Academic, New York, pp 313–362
22. Hager EA (2004) Composite gelatin delivery system for bone regeneration. Massachusetts Institute of Technology, Cambridge
23. Jussila J, Leppaniemi A, Paronen M, Kulomaki E (2005) Ballistic skin simulant. Forensic Sci Int 150(1):63–71
24. Sunaga T, Ikehira H, Furukawa S, Tamura M, Yoshitome E, Obata T et al (2003) Development of a dielectric equivalent gel for better

impedance matching for human skin. Bioelectromagnetics 24 (3):214–217
25. Ulubayram K, Aksu E, Gurhan SID, Serbetci K, Hasirci N (2002) Cytotoxicity evaluation of gelatin sponges prepared with different cross-linking agents. J Biomater Sci Polym Ed 13(11):1203–1219
26. Ankersen J, Birkbeck AE, Thomson RD, Vanezis P (1999) Puncture resistance and tensile strength of skin simulants. Proc Inst Mech Eng [H] 213(H6):493–501
27. Manschot JFM, Brakkee AJM (1986) The measurement and modelling of the mechanical properties of human skin *in vivo*. I. The measurement. J Biomech 19(7):511–515
28. Abanto-Bueno J, Lambros J (2002) Investigation of crack growth in functionally graded materials using digital image correlation. Eng Fract Mech 69(14–16):1695–1711
29. Abanto-Bueno J, Lambros J (2005) Experimental determination of cohesive failure properties of a photodegradable copolymer. Proc Soc Exp Mech 52:144–152
30. Berfield T, Patel J, Shimmin R, Braun P, Lambros J, Sottos N (2007) Micro- and nanoscale deformation measurement of surface and internal planes via digital image correlation. Exp Mech 47(1):51–62
31. Berfield TA, Patel JK, Shimmin RG, Braun PV, Lambros J, Sottos NR (2006) Fluorescent image correlation for nanoscale deformation measurements. Small 2(5):631–635
32. Hall TJ, Bilgen M, Insana MF, Krouskop TA (1997) Phantom materials for elastography. IEEE Trans Ultrason Ferroelectr Freq Control 44(6):1355–1365
33. McDermott MK, Chen TH, Williams CM, Markley KM, Payne GF (2004) Mechanical properties of biomimetic tissue adhesive based on the microbial transglutaminase-catalyzed crosslinking of gelatin. Biomacromolecules 5(4):1270–1279
34. Knauss WG, Chasiotis I, Huang Y (2003) Mechanical measurements at the micron and nanometer scales. Mech Mater 35(3–6):217–231
35. Rao SS (2002) Applied numerical methods for engineers and scientists. Prentice Hall, Upper Saddle River
36. Muskhelishvili NI (1953) Some basic problems of the mathematical theory of elasticity, 3rd edn. Noordhoff, Groningen
37. Krehbiel JD (2008) Digital image correlation for improved detection of basal cell carcinoma. University of Illinois, Urbana